



CHORUS

This is the accepted manuscript made available via CHORUS. The article has been published as:

Short-range thermal magnon diffusion in magnetic garnet

K. An, R. Kohno, N. Thiery, D. Reitz, L. Vila, V. V. Naletov, N. Beaulieu, J. Ben Youssef, G. de Loubens, Y. Tserkovnyak, and O. Klein

Phys. Rev. B **103**, 174432 — Published 26 May 2021

DOI: [10.1103/PhysRevB.103.174432](https://doi.org/10.1103/PhysRevB.103.174432)

Short-range Thermal Magnon Diffusion in Magnetic Garnet

K. An,^{1,*} R. Kohno,¹ N. Thiery,¹ D. Reitz,² L. Vila,¹ V. V. Naletov,^{1,3} N. Beaulieu,^{4,5} J. Ben Youssef,⁵ G. de Loubens,⁴ Y. Tserkovnyak,² and O. Klein^{1,†}

¹*Universit Grenoble Alpes, CEA, CNRS, Grenoble INP, Spintec, 38054 Grenoble, France*

²*Department of Physics and Astronomy, University of California, Los Angeles, California 90095, USA*

³*Institute of Physics, Kazan Federal University, Kazan 420008, Russian Federation*

⁴*SPEC, CEA-Saclay, CNRS, Université Paris-Saclay, 91191 Gif-sur-Yvette, France*

⁵*LabSTICC, CNRS, Université de Bretagne Occidentale, 29238 Brest, France*

(Dated: May 4, 2021)

Using the spin Seebeck effect (SSE), we study the propagation distance of thermally-induced spin currents inside a magnetic insulator thin film in the short-range regime. We disambiguate spin currents driven by temperature and chemical potential gradients by comparing the SSE signal before and after adding a heat-sinking capping layer on the same device. We report that the measured spin decay behavior near the heat source is well accounted for by a diffusion model where the magnon diffusion length is in submicron range, *i.e.* two orders of magnitude smaller than previous estimates inferred from the long-range behavior. Our results highlight the caveat in applying a diffusive theory to describe thermally generated magnon transport, where a single decay length may not capture the behavior on all length scales.

I. INTRODUCTION

The generation of pure spin currents by heat [1, 2] is a tantalizing subject, which offers a unique opportunity to reach strong out-of-equilibrium regime with large spin current density produced inside a magnetic material [3]. Interests lie in the prospect of reaching new collective dynamical behaviors of spin transport such as the hydrodynamic regime conspicuous by the emergence of turbulences [4]. Magnon superfluidity may even establish when the density exceeds the Bose-Einstein condensation threshold under large temperature gradients applied to low damping magnetic insulators, such as yttrium iron garnets (YIG) [5, 6], where local heating can be provided by injecting a large electrical current density through an adjacent metal, advantageously in Pt [7–9], or by optically heating with a laser [10–12].

The spin transport properties are governed by λ , the characteristic length over which spin is conserved. Previous reports on measuring λ in YIG at room temperature by the spin Seebeck effect (SSE) indicates that for distances larger than $\sim 10 \mu\text{m}$ (long-range regime), the SSE signal follows an exponential decay with a characteristic length of the order of $\lambda_0 \approx 10 \mu\text{m}$ [13, 14]. This large value is believed to exceed ℓ , the magnon mean free path, which is expected to be much shorter than λ_0 [15, 16], suggesting there that magnons behave as a diffusive gas [17]. However such a large value of λ_0 may seem surprising for *thermal magnons* [18]. If one extends the magnon dispersion up to the THz-range, the extrapolated ballistic decay length for thermal magnons is $\lambda_{\text{bal}} = \lambda_{\text{ex}} / (2\alpha\sqrt{\omega_T/\omega_M}) = 2 \mu\text{m}$, where $\omega_T = k_B T_0 / \hbar = 2\pi \times 6.25 \text{ THz}$, T_0 is room temperature, $\lambda_{\text{ex}} \approx 15 \text{ nm}$ is the exchange length in YIG, $\alpha \approx 10^{-4}$ [19] is the Gilbert damping, and $\omega_M = \gamma\mu_0 M(T_0) = 2\pi \times 4.48 \text{ GHz}$, with M being the saturation magnetization. This estimate λ_{bal} , which is already

smaller than λ_0 , should be considered as an upper bound because *i)* the Gilbert damping is expected to be increased in the THz-range [20] *ii)* the group velocity is reduced towards the edge of the Brillouin zone [21, 22], and *iii)* it does not account for the $\sqrt{\ell/\lambda_{\text{bal}}}$ reduction of the characteristic propagation distance due to diffusion process.

In fact, the distance range of the transport study is also a potent means to select a very specific part of the magnon spectrum. In experiments focusing on the long-range behavior, one has in essence efficiently filtered out any short decay magnons. Behind this debate lies a fundamental question of how well magnon transport can be described by a diffusive model forming one gas with a single λ , whose value would govern SSE on all length scales. Submicron lengths have been inferred from several longitudinal SSE measurements in the spatial [23, 24] and temporal domains [11, 25]. In nonlocal SSE measurements, where two different Pt strips are used for the spin injection and detection, only longer spin decay lengths have been reported. The existence of shorter decay lengths has been difficult to observe because the voltage induced by SSE shows a nontrivial spatial decay as a function of the Pt detector position near the heat source [4, 26]. The complex decay profile can be attributed to the competition between magnons driven by the gradients of temperature and magnon chemical potential [17, 27, 28]. It has been difficult to control these two sources of spin excitation in experiments, which hinders a correct extraction of a characteristic decay length near the heat source. In this paper we develop a way to disambiguate these two contributions after altering the temperature profile. We monitor on the same devices the short-range SSE signal before (case A) and after (case B) capping it with a non-magnetic aluminum layer. The capping allows to change the vertical thermal gradient without altering the

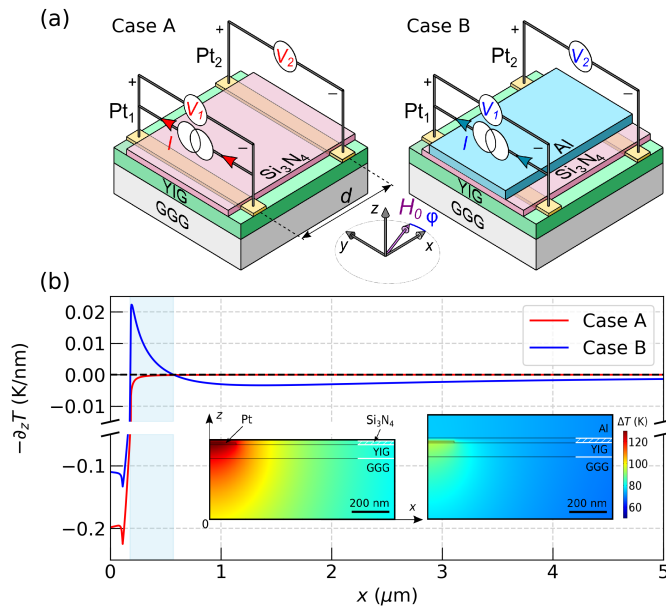


FIG. 1. (a) Comparison of the measurements of the local (V_1) and nonlocal (V_2) voltages generated in YIG|Pt| Si_3N_4 (case A) and YIG|Pt| Si_3N_4 |Al (case B) stacks. Experiments are performed on the same devices before and after the deposition of an Al capping layer (left and right schematics). Two Pt electrodes deposited on top of YIG film monitor the spin-transconductance when an external magnetic field H_0 rotates in-plane in the azimuthal direction φ . The center-to-center distance d between the two electrodes is varied between $0.5 \mu\text{m}$ to $6.3 \mu\text{m}$. (b) Calculated vertical temperature gradient profiles at the top YIG surface at 2 mA. The light blue shaded region indicates the inverted gradient in case B. Beyond this region, $\partial_z T$ is about three orders of magnitude larger in case B. The insets are the calculated temperature profiles for both cases.

YIG interface. We observe that the sign of SSE voltage inverts twice within a distance of $1 \mu\text{m}$ from the heat source for case B. The corresponding sign reversal of SSE suggests that the magnons clearly sense the change in local temperature gradient taking place for case B. With a simple diffusive transport model, the measured SSE decay profile for both cases can be reproduced if one introduces a thermal magnon diffusion length $\lambda \approx 300 \pm 200 \text{ nm}$. The extracted short λ from our measurement fills the gap between different length scales reported in the longitudinal and nonlocal SSE measurements.

II. EXPERIMENT

We use a 56 nm thick YIG(111) film grown on a $500 \mu\text{m}$ GGG substrate by liquid phase epitaxy. Ferromagnetic resonance experiments have shown a damping parameter of 2×10^{-4} revealing an excellent crystal quality of the YIG film [29]. The sample structure and measurement configuration are shown in Fig. 1(a). In our notation,

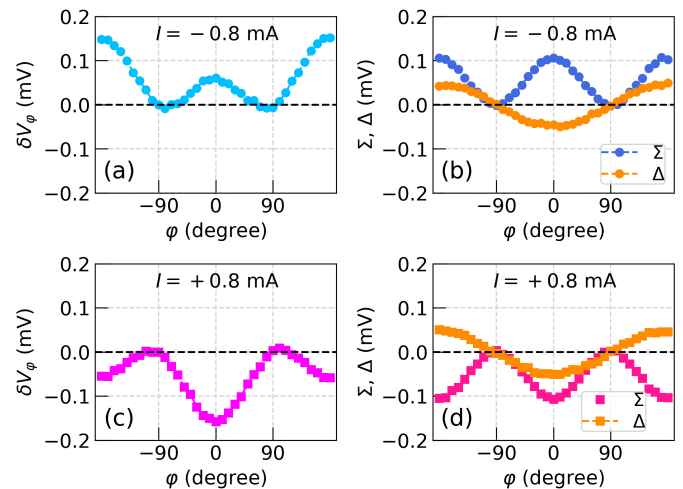


FIG. 2. (a,c) Angular dependence of the background subtracted local voltage δV_φ measured in the Pt injector strip for the current of $I = \pm 0.8 \text{ mA}$ and external magnetic field of $\mu_0 H_0 = 200 \text{ mT}$. We subtract the reference voltage V_y from the raw signal to remove any contributions not associated with magnons. In (b) and (d) we decompose the measured magnetoresistive voltage into two components: Σ and Δ , the even and odd contributions of the signal with respect to the mirror symmetry along the yz plane (see the text).

subscripts 1 and 2 refer to the voltages measured by the Pt_1 and Pt_2 , respectively. We show the data for both YIG|Pt| Si_3N_4 (case A, red) and YIG|Pt| Si_3N_4 |Al (case B, blue). The color conventions will be used consistently throughout the paper. Two Pt strips (Pt_1 and Pt_2) with width of 300 nm , length of $30 \mu\text{m}$ and thickness of 7 nm have been evaporated directly on top of the YIG film. The center-to-center distance d between two Pt strips varies from 0.5 to $6.3 \mu\text{m}$. The sample is then covered by a 20 nm thick Si_3N_4 protection film. A local Joule annealing was used to enhance the spin conductance [30]. After full characterization of the different devices, a 105 nm thick Aluminum layer with length $30 \mu\text{m}$ and width $10 \mu\text{m}$ is deposited on the top of the Si_3N_4 film, and the same devices are measured again. The sample is submitted to an external field of $\mu_0 H_0 = 200 \text{ mT}$ rotating within the xy plane (in-plane configuration). We first show the expected change in temperature profile by the Al capping in Fig. 1(b). The temperature rise, ΔT , is about 40 K lower in case B at the Pt injector. The reduced temperature rise is experimentally confirmed by measuring the Pt_1 resistance (see Appendix A). Besides the change in the temperature profile, the gradient profile also shows a dramatic change. While in case A the thermal gradient is always directed downwards (into the substrate), in case B, a large thermal gradient directed upwards (into Al) is created half a micron away from the source. The shaded region highlights the effect. Since the vertical thermal gradient drives the SSE, this feature gives rise to

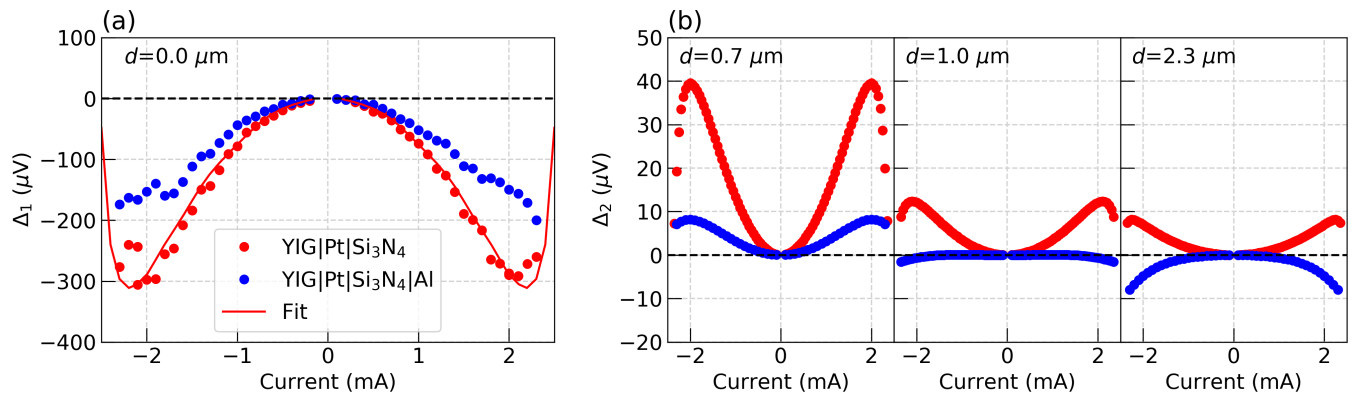


FIG. 3. (a) Current dependence of measured local Δ_1 for case A (YIG|Pt|Si₃N₄) and case B (YIG|Pt|Si₃N₄|Al). The red solid line shows that the local Δ_1 follows the expected behavior based on the temperature rise with increasing current. (b) Measured current dependence of nonlocal Δ_2 for three different d 's for the case A (red) and B (blue).

an additional signal at Pt₂.

We use the same method demonstrated in our previous work to extract the SSE voltage [8]. As an illustration, we display the background-subtracted local voltage $\delta V_\varphi = V_\varphi - V_y$ measured with the Pt injector on YIG|Pt|Si₃N₄ at ± 0.8 mA as a function of the in-plane magnetic field angle φ in Fig. 2(a). The offset V_y , measured when the magnetic field is applied along the y axis ($\varphi = 90^\circ$), takes account of all the spurious contributions to the spin transport [31]. To distinguish the SSE from the spin orbit torque, we define two quantities based on the yz mirror symmetry: $\Sigma_{\varphi,I}, \Delta_{\varphi,I} \equiv (\delta V_{\varphi,I} \pm \delta V_{\bar{\varphi},I})/2$ where $\bar{\varphi} = \pi - \varphi$ [32]. Figure 2(b) and (c) show the evolution of the extracted Σ and Δ as a function of φ for both polarities of the current I . Σ is antisymmetric with respect to the current and evolves as $\cos 2\varphi$, as expected from the spin Hall magnetoresistance effect [33–35]. Δ shows a $\cos \varphi$ angular dependence and is symmetric with respect to the current, consistent with the SSE [36]. In the following, we shall exclusively focus on the SSE voltage (Δ).

Next, we compare the full current dependence of the SSE voltage $\Delta_1(I)$ ($\Delta_{\varphi=0,I}$ in Pt₁) for both case A (red) and case B (blue) in Fig. 3(a). We clearly see that the voltage is negative for both cases over the entire current range. The parabolic curvature observed at low currents decreases when the Al heat sink is introduced, which agrees with the reduced temperature rise. We observe that $\Delta_1(I)$ reaches a minimum at 2 mA for case A with the minimum shifting to a higher current for case B. We attribute this reversal of the slope as the growing influence of the vanishing YIG magnetization as one approaches the Curie temperature $T_c = 544$ K determined on our garnet film, which is close to the literature value of bulk YIG [37]. The current dependence of $\Delta_1(I)$ for case A can be reproduced by an empirical formula $\Delta_1 \propto SM(T)(T - T_0)$, where S is the spin Seebeck coefficient, $M(T)$ is the saturation magnetization at the temperature T , while $T_0 = 300$ K is the temperature of

the substrate. From the fit as shown in Fig. 3(a) one can extract $S \approx 0.08 \mu\text{V K}^{-1}$ in good agreement with previous estimates [38] (see Appendix C). In case A (red curves in Fig. 3(b)), the sign of the measured voltage changes from negative to positive when going from the local voltage Δ_1 to the non-local voltage Δ_2 , respectively. This observation is consistent with the previous works that reported a single sign reversal of the SSE voltage measured as a function of distance from the heat source [26, 39, 40]. It has been reported that the characteristic distance at which the magnon accumulation changes the sign can be tuned by varying the magnetic film thickness [26] or magnon diffusion length [39]. The situation is quite different for case B, as shown with the blue dots in Fig. 3(b). In the vicinity of the injector, the nonlocal Δ_2 is still positive at $0.7 \mu\text{m}$ but much smaller than case A. The sign of Δ_2 for case B eventually becomes negative when the Pt detectors are positioned at $1 \mu\text{m}$ and $2.3 \mu\text{m}$ away from the injector. Our understanding of the sign changes as a function of d is as follows: at $d = 0$, heat drags magnons from Pt₁ down into YIG (negative sign SSE); at larger d , magnons can transfer spin from the YIG bulk into Pt₂ (positive sign); adding Al creates a region of inverted heat flow over a short range (positive sign within 0.2 and $0.5 \mu\text{m}$) and significant heat flow down into YIG over a longer range (negative sign). The fact that we see a negative signal after the second crossing signifies that the positive SSE driven by the magnon diffusion already becomes diminished and the local temperature driven SSE dominates. In this perspective the second crossing point may put a constraint on the estimate of the thermal magnon diffusion length.

III. MODELING

To model our experiment, we treat the magnons in YIG as a diffusive gas with temperature T and chemical

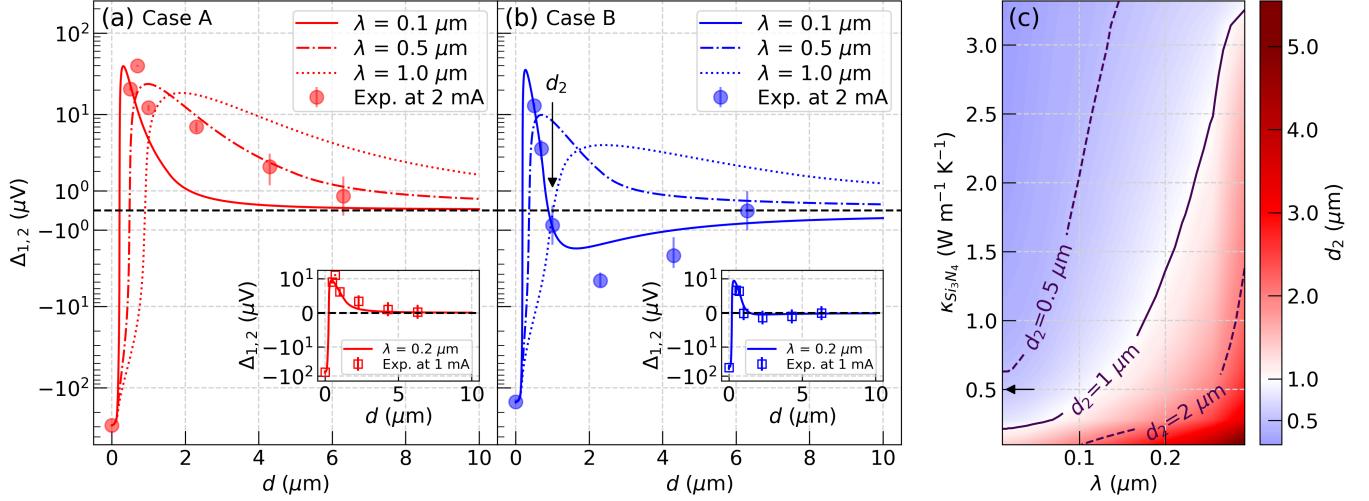


FIG. 4. Comparison of the experimentally measured Δ 's at 2 mA with the numerically calculated chemical potential profile for (a) case A and (b) case B on a symmetric log scale. The result with $\lambda = 0.1 \mu\text{m}$ reproduces the measured double crossing as shown in (b). The second crossing does not appear anymore when increasing λ to 0.5 or 1 μm . Insets show the data taken at 1 mA compared with the calculations with $\lambda = 0.2 \mu\text{m}$. (c) Contour plot of the second crossing position d_2 as a function of λ and thermal conductivity of Si_3N_4 . The black lines represent the iso-lines for different d_2 's. The arrow points to the value of $\kappa_{\text{Si}_3\text{N}_4}$ used in panel (a) and (b).

potential μ described by a set of transport coefficients [17]. The measured Δ signal is proportional to the magnon chemical potential at the interface between YIG and Pt [41]. The continuity equation for spin current density J_s in the steady state is

$$-\nabla \cdot \mathbf{J}_s = g\mu, \quad (1)$$

where g is spin relaxation coefficient. In linear response, the transport equation is

$$\mathbf{J}_s = -\sigma(\nabla\mu + \zeta\nabla T), \quad (2)$$

where σ is the spin conductivity and ζ is the bulk spin Seebeck coefficient. The two equations are combined and lead to

$$\frac{\mu}{\lambda^2} = \nabla^2\mu + \zeta\nabla^2 T, \quad (3)$$

where $\lambda = \sqrt{\sigma/g}$ is the thermal magnon diffusion length.

We use a finite element method, COMSOL, to calculate the temperature profile and the magnon chemical potential μ in 3D assuming translational invariance along the y axis (see Appendix B). The second crossing point d_2 observed in the case B, as indicated in Fig. 4(b), is an important feature that reveals the inverted heat flow near the heat source as shown in Fig. 1(b). The calculated spatial profiles of μ for three different values of λ are compared with the experimental data in Figs. 4(a) and (b) after normalization to the measured values at $d = 0 \mu\text{m}$. We find that the second sign reversal at d_2 can be reproduced with a short $\lambda = 100 \text{ nm}$. Increasing it to 0.5 or 1 μm , however, no longer reproduces the second

crossing in case B (compare solid line with dashed and dotted lines in Fig. 4(b)). In the insets of Fig. 4, we present the best fit obtained with $\lambda = 0.2 \mu\text{m}$ for the data taken at 1 mA. Although the Δ signal seems to depend on the current value, the extracted λ is not significantly modified (see Appendix E).

The fit value of λ depends on other parameters in the model. The second crossing point, d_2 , can be affected by the temperature profile at the interface, which is sensitive for example to the thermal conductivity of Si_3N_4 . We show a contour plot for d_2 as a function of $\kappa_{\text{Si}_3\text{N}_4}$ and λ in Fig. 4(c). The measured second crossing constrains the parameter space to the line along $d_2 = 1 \mu\text{m}$. The second crossing is not observed for $\lambda > 500 \text{ nm}$ regardless of $\kappa_{\text{Si}_3\text{N}_4}$. These considerations can be further modified by the interfacial SSE due to the magnon-phonon temperature difference at the interface [42, 43]. Enhanced local temperature driven contribution to the measured signal can increase λ for a given d_2 . To have *quantitative* agreement with the data, we also get an upper bound of $\lambda \sim 500 \text{ nm}$, although it is worth to mention that in the limit of large temperature mismatch between magnons in YIG and the Pt one can *qualitatively* reproduce the single crossing in case A and double crossing in case B for much larger λ (see Appendix D).

Although our proposed fit with a diffusive equation parametrized by $\lambda \in [100, 500] \approx 300 \pm 200 \text{ nm}$ captures well the short-range behavior in both cases A and B, we emphasize that this does not contradict earlier works [13, 44]. The data observed for case A are similar to the one already observed in other YIG devices, where the fit

of the long-range decay behavior has lead to the larger $\lambda_0 \approx 30 \times \lambda$ [45]. We note that the magnon diffusion equation (Eq. 3) is constructed under the assumption of a long-distance behavior, where all the magnons are equilibrated to a common chemical potential. It is not surprising, however, to have a significant departure in the spin-transport behavior at short distances, where magnons are not yet internally equilibrated or thermally equilibrated with the surrounding phonons [24]. In certain special cases nonetheless, this may be modeled by introducing effective length scales, which is illustrated in our analysis. Specifically, we suggest a possibility that a subset of out-of-equilibrium magnons, from the thermal energy range, is locally decaying on a shorter length scale (λ) than the asymptotic long-distance decay (λ_0). We note that our extracted λ is close to the value for the magnon diffusion length predicted in a previous work [46], while λ_0 is comparable to the prediction of Ref. [47]. The previously reported energy relaxation length of magnons [11, 23–25] is also seen to be similar to λ , where the possible connection needs to be further explored.

IV. CONCLUSIONS

In summary, we measured the spatial distribution of thermally generated magnons in a thin YIG film. We altered the temperature profile across the YIG film with an aluminum layer. The results are that the non-equilibrium thermal magnon profile deviates from an exponential decay and shows a double sign reversal. We use a linear response magnon transport theory to obtain the short-range thermal magnon diffusion length of a submicron range, which is about two orders of magnitude smaller than the value found in previous reports focused on the long-range measurements. Our results suggest that the local effect of heating is to produce magnons which decay on a short length scale near the source. The experimental approach using a heat sink to reveal a short magnon diffusion length may find applications to other systems, especially when the length scale of the diffusion and temperature gradient are comparable.

ACKNOWLEDGMENTS

This work was supported in part by the Grants No.18-CE24-0021 from the ANR of France. K.A. acknowledges support from the National Research Foundation of Korea (NRF) grant (No. 2021R1C1C201226911) funded by the Korean government (MSIT). V.V.N. acknowledges support from UGA through the invited Prof. program and from the Russian Competitive Growth of KFU.

APPENDIX

Appendix A: Temperature characterization

We characterize the temperature rise induced by Joule heating using the Pt resistance as a temperature sensor. The Pt injector is connected to a 6221 Keithley, which generates a 10 ms pulse current with a duty cycle of 10%. The voltages are measured with a 2182A Keithley nano-voltmeter [8]. In the inset of Fig. 5 we plot the rational increase of Pt resistance as a function of ambient temperature between 220 and 300 K. The change in resistance ΔR is linearly proportional to the temperature rise $\Delta T = T - T_0$, i.e., $\Delta R(T)/R_0 = \zeta \Delta T$, where R_0 is the initial resistance and ζ is the thermal coefficient of resistance and $T_0 = 300$ K is room temperature. We obtain $\zeta = (2.1 \pm 0.3) \times 10^{-3} \text{ K}^{-1}$ for our Pt strip from the fit. The increase of resistance and corresponding temperature rise as a function of current are plotted in Fig. 5. The Pt temperature increases quadratically with applying current owing to the Joule heating ($\propto I^2$). The temperature rise in Pt is about 45 K lower after the Al deposition at 2 mA (current density of $\sim 10^{12} \text{ A/m}^2$). This indicates that the Al layer effectively spreads the heat from the Pt injector.

Appendix B: Details of theoretical calculation

The temperature profiles and the chemical potential are calculated in a 2D geometry using a finite element method, COMSOL. We choose a boundary condition that the top and side surfaces are thermally isolated and the bottom is held at room temperature, and the normal component of the spin current is zero at the boundary.

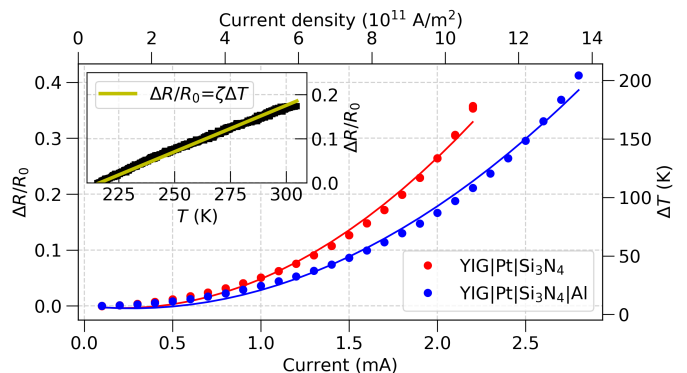


FIG. 5. Resistance increase and the corresponding temperature elevation in the Pt strip as a function of the injected current with and without Al capping (red and blue dots, respectively). The solid red and blue lines are quadratic fits to the data. The inset shows the temperature dependence of Pt resistance. The yellow line is a linear fit to the data.

The geometry was chosen to be the same as the actual sample size except that the lateral size of sample and the thickness of GGG are reduced to $30 \mu\text{m}$ to facilitate the calculation. The thermal conductivity parameters are 9, 7.4, 29, 220, and $0.5 \text{ Wm}^{-1}\text{K}^{-1}$ for GGG [48], YIG [48], Pt [49], Al [50], and Si_3N_4 [51], respectively. The value of the spin Seebeck coefficient ς does not affect the decay profile. The thermal magnon diffusion length λ is varied. The calculated temperature profiles at the top of YIG surface are shown for the two cases in Fig. 6. The temperature difference at $d = 0 \mu\text{m}$ (the center of Pt injector strip) between two cases is 37 K, which roughly agrees with the measured temperature difference at 2 mA as shown in Fig. 5. To check the validity of calculated temperature profile, we measured the temperature rise at the position of the detector in case A. Our estimation yields a temperature drop of 46% for the detector placed at $d = 0.5 \mu\text{m}$ away from the injector. This is larger than the simulated temperature drop of 30% over the same distance (red curve in Fig. 6). The discrepancy may arise from (1) the simplification to 2D modeling, (2) possible difference in parameters between the simulation and measurement. Also the heat could be removed by the Pt detector, which is not taken account in this calculation. However we find that the temperature change due to the presence of Pt detector is negligible (see Appendix F).

Appendix C: Temperature dependence of the local SSE voltage

In Fig. 3(a), we fit the measured current dependence of Δ_1 for case A. The measured local SSE voltage follows the analytical expression $\Delta_1 = SL_{\text{Pt}} \langle \partial_z T \rangle$, where S is the spin Seebeck coefficient, L_{Pt} is the length of the Pt electrode, and $\langle \partial_z T \rangle$ is the vertical temperature gradient across the YIG thickness. The latter is proportional to the temperature rise of the Pt injector: $\langle \partial_z T \rangle = (T - T_0)/l_T$, where $T_0 = 300 \text{ K}$ is the substrate temperature and l_T is the characteristic decay length of temperature from the

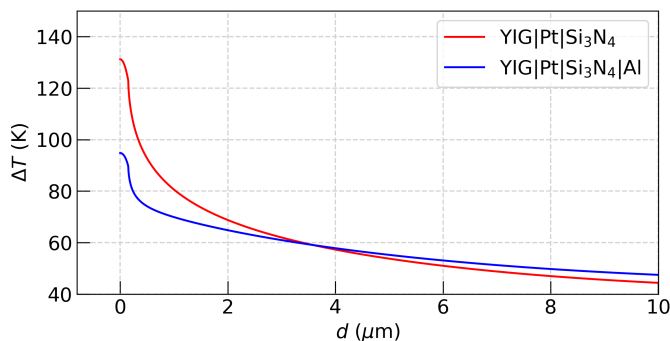


FIG. 6. Calculated temperature rise profiles for two cases with and without the Al layer at 2 mA.

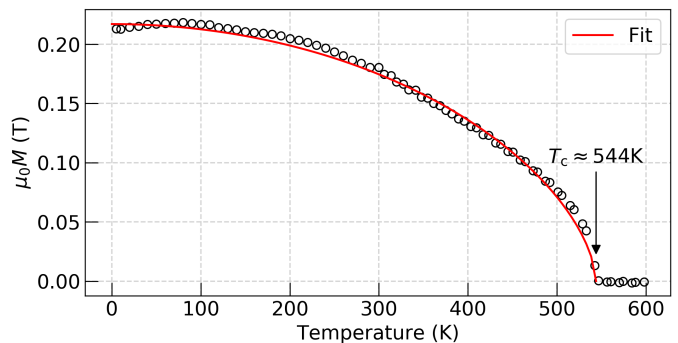


FIG. 7. Measured temperature dependence of magnetization. The red solid line is a fit with Eq. A2.

top surface. By comparing the measured Pt temperature rise $T - T_0 = 130 \text{ K}$ at 2 mA with the expected $\langle \partial_z T \rangle = 10 \text{ K}/56 \text{ nm}$ as shown in Fig. 1(b), we obtain $l_T \sim 730 \text{ nm}$. Assuming that the temperature dependence of S is simply due to $\mu_0 M(T)$ (in contrast with the fitted temperature dependence used in a previous work [52]), the expression for Δ_1 becomes

$$\Delta_1(T) = C \frac{L_{\text{Pt}}}{l_T} (T - T_0) \mu_0 M(T), \quad (\text{A1})$$

where $C \equiv S/(\mu_0 M(T))$. The temperature dependence of magnetization follows an empirical formula,

$$\mu_0 M(T) = \mu_0 M_0 (1 - (T/T_c)^a)^b, \quad (\text{A2})$$

where $\mu_0 M_0 = 0.217 \text{ T}$ is the YIG saturation magnetization at $T = 0 \text{ K}$, while the exponents $a = 2.0$ and $b = 0.6$ are extracted from the fit as shown in Fig. 7. The expression for $\Delta_1(T)$ is converted to $\Delta_1(I)$ using the temperature-current calibration curve in Fig. 5. Then we use C as a single fitting parameter to reproduce the observed behavior (solid red line in Fig. 3(a)). The fit yields $C = 0.43 \mu\text{V K}^{-1} \text{ T}^{-1}$. At room temperature, where the magnetization of YIG is about 0.178 T, the spin Seebeck coefficient of our YIG|Pt system is about $S \approx 0.08 \mu\text{V K}^{-1}$, which agrees with a previous work [38].

Appendix D: Interfacial effect

Another potential source of spin currents to consider are interfacial effects at the Pt strips arising from the Kapitza resistance, which creates a temperature discontinuity, δT across the YIG|Pt interface [43, 53]. One can assume that δT is proportional to the temperature gradient at the interface, $\partial_z T$. The measured SSE voltage including the interfacial contribution can be written

$$V_{\text{SSE}} = C_1(\mu - C_2 k_B \partial_z T), \quad (\text{A3})$$

where μ is the magnon chemical potential obtained by solving Eq. (3). Here we are interested in the spin flow to

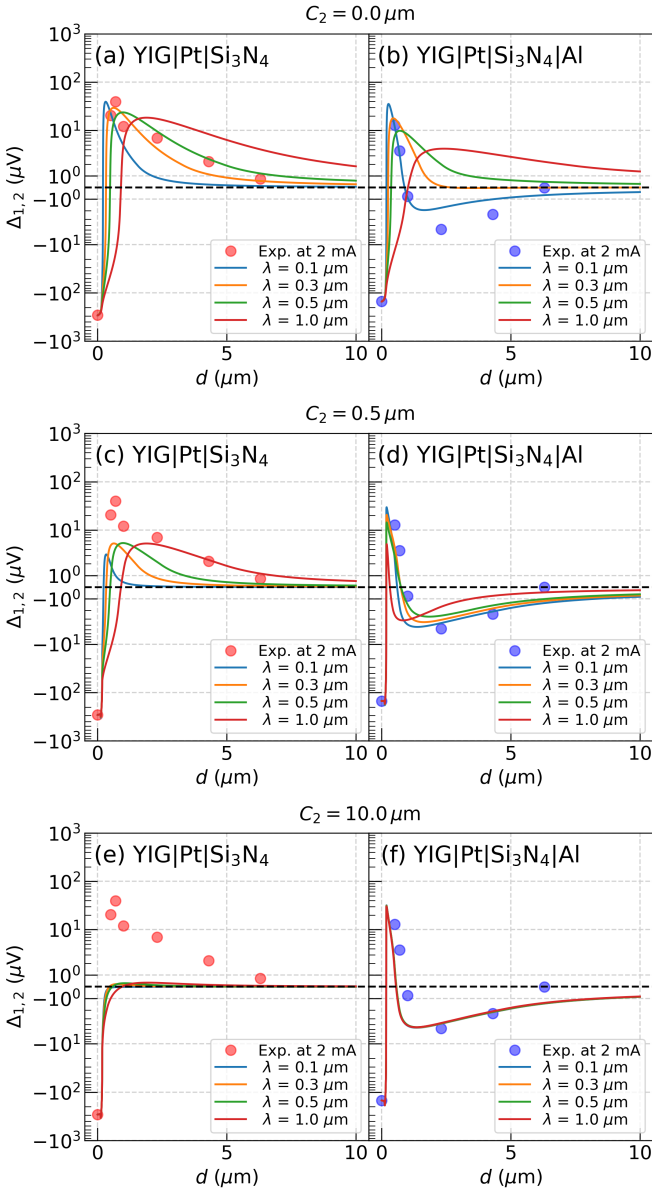


FIG. 8. The calculated spatial profile of μ after normalization to the measured local Δ_1 . The results are compared to the measured Δ 's with varying λ for (a,c,e) case A and (b,d,f) case B with $C_2 = 0, 0.5, 10 \mu\text{m}$. Only $\lambda = 100$ and 300 nm show qualitative agreements for case B with $C_2 = 0$. With $C_2 = 0.5 \mu\text{m}$, $\lambda = 500 \text{ nm}$ gives rough agreements for both cases (c and d). However $\lambda = 1 \mu\text{m}$ does not fit neither the first crossing in case A nor the second crossing in case B well. The fit does not work for case A anymore with $C_2 = 10 \mu\text{m}$ even though the double crossing in case B can be reproduced (e and f).

leading order in the spin exchange coupling across YIG|Pt interface. In this case, T and μ are calculated in the absence of spin flow into Pt. The two are evaluated along the top YIG surface. C_1 is a constant, which normalizes the simulation results to the experimental data at $d = 0 \mu\text{m}$. C_2 is a parameter proportional to the Kapitza length,

which represents the contribution of the interfacial term. The negative sign implies that the heat flow is along the opposite direction of the temperature gradient. One can assume that C_2 is the same for both case A and case B for fixed d because the Al layer does not touch either the YIG or Pt directly. We recall also that in our cartesian frame z is the direction normal to the film.

Figure 8 shows the effect of adding a finite C_2 for different values of λ . For $C_2 = 0.5 \mu\text{m}$, the calculation can reproduce the observed double crossing in case B for all four values of λ . However $\lambda = 1 \mu\text{m}$ case does not predict well either the observed first crossing in case A or the second crossing in case B. It is important to also point out that V_{SSE} eventually follows the temperature gradient profile in Fig. 1(b) when the C_2 term is dominant (Fig. 8(f)) even for large values of λ . Thus in the limit of very large C_2 , the observation of a double SSE sign crossing in case B is not anymore conspicuous of a short decay length of thermal magnons. Another consequence of assuming that the interfacial effects are dominant, is to reduce strongly (more than three orders of magnitude) the amplitude of the signal after the first crossing in case A. The fact that we observe experimentally only an order of magnitude reduction of the SSE signal for case A thus points to a small value of $C_2 \ll 0.5 \mu\text{m}$ (see Fig. 3 between $d = 0$ and $d = 0.7 \mu\text{m}$). Experimentally, we have performed an estimation of the Kapitza resistance by comparing the increase of the Pt temperature inferred from the variation of its resistance and the temperature increase of YIG inferred from the decrease of the Kittel frequency due to a change of $M_s(T)$, whose slope is about 0.4 mT/K at room temperature [8]. We have found no temperature difference between the Pt and the YIG underneath within the uncertainty of 2 K when the increase of temperature rise is $T - T_0 = 70 \text{ K}$. At 2 mA , where $T - T_0 = 130 \text{ K}$, the temperature gradient is 0.2 K/nm . From this, we estimate an upper bound of Kapitza length of about 20 nm .

Appendix E: Current dependence of λ

Experimentally we find that the Δ signal seems to increase with current (see the data points in Fig. 9). However when quantitatively checking if λ depends on the value of current, we find that the best fitting λ is not significantly modified with current. In Fig. 9(a), we show that $\lambda = 0.4 \mu\text{m}$ fits very well both data sets taken at 1 mA and 2 mA . In case B, $\lambda = 0.1 \mu\text{m}$ fits both data sets reasonably (Fig. 9(b)). We note that all these λ 's are within our uncertainty range, i.e., $\lambda \in [100, 500] \text{ nm}$. Also the Δ signal in case B becomes more negative with increasing current. We believe this is because the Δ contribution by the temperature gradient prevails over the magnon diffusion process at higher currents leading to the more negative signal.

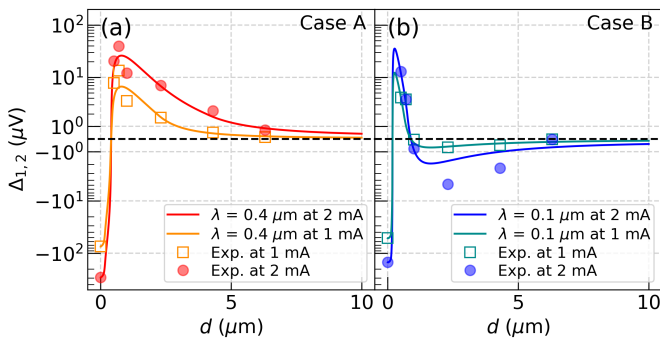


FIG. 9. Experimental data at 1 mA and 2 mA are plotted. (a) Red (orange) line is the calculated decay profile for 2 mA (1 mA) with $\lambda = 0.4 \mu\text{m}$ and $C_2 = 0$. (b) Similar plots are shown for case B, where blue and cyan solid lines are the calculated profiles for 2 mA and 1 mA, respectively, with $\lambda = 0.1 \mu\text{m}$ and $C_2 = 0$. The calculations are normalized to the measured local Δ_1 .

Appendix F: Effect of Pt detector on temperature profile

Finally we consider the effect of Pt detector on the temperature profile. In Fig. 10, we compare the calculated temperature profiles with/without the Pt detector at $d = 1 \mu\text{m}$. There are less than 1 K variations of temperature due the Pt detector in both cases, which amount to less than 1% change in the temperature rise. This is because (1) the Pt strip covers only a small fraction of YIG surface and (2) thermal conductivity of our 7 nm thick Pt is estimated to be low as about $29 \text{ W m}^{-1}\text{K}^{-1}$ expected from the high resistance of $3.8 \text{ k}\Omega$, consistent with Wiedemann-Franz law. Compared to the temperature change induced by the Al layer, this temperature change is negligible. Therefore the Pt detector is not included in the calculations.

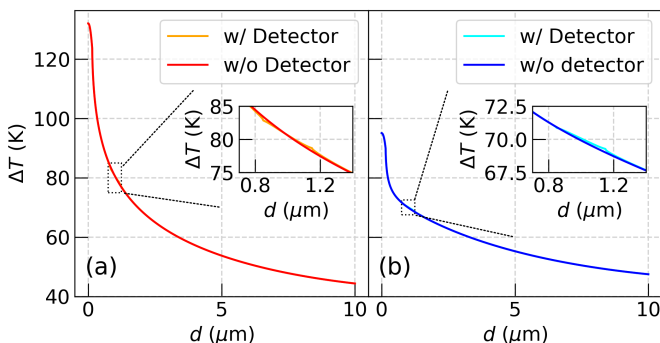


FIG. 10. Comparison of calculated temperature profiles at 2 mA with and without Pt detector at $1 \mu\text{m}$ for (a) case A and (b) case B.

* Current address: Quantum Spin Team, Korea Research Institute of Standards and Science, Daejeon, Republic of Korea

† Corresponding author: oklein@cea.fr

- [1] G. E. Bauer, E. Saitoh, and B. J. Van Wees, Spin caloritronics, *Nat. Mater.* **11**, 391 (2012).
- [2] S. R. Boona, R. C. Myers, and J. P. Heremans, Spin caloritronics, *Energy Environ. Sci.* **7**, 885 (2014).
- [3] M. Weiler, M. Althammer, M. Schreier, J. Lotze, M. Pernpeintner, S. Meyer, H. Huebl, R. Gross, A. Kamra, J. Xiao, *et al.*, Experimental test of the spin mixing interface conductivity concept, *Phys. Rev. Lett.* **111**, 176601 (2013).
- [4] C. Ulloa, A. Tomadin, J. Shan, M. Polini, B. Van Wees, and R. Duine, Nonlocal spin transport as a probe of viscous magnon fluids, *Phys. Rev. Lett.* **123**, 117203 (2019).
- [5] S. A. Bender, R. A. Duine, and Y. Tserkovnyak, Electronic pumping of quasiequilibrium bose-einstein-condensed magnons, *Phys. Rev. Lett.* **108**, 246601 (2012).
- [6] Y. Tserkovnyak, S. A. Bender, R. A. Duine, and B. Flebus, Bose-einstein condensation of magnons pumped by the bulk spin seebeck effect, *Phys. Rev. B* **93**, 100402 (2016).
- [7] C. Safranski, I. Barsukov, H. K. Lee, T. Schneider, A. Jara, A. Smith, H. Chang, K. Lenz, J. Lindner, Y. Tserkovnyak, *et al.*, Spin caloritronic nano-oscillator, *Nat. Commun.* **8**, 1 (2017).
- [8] N. Thiery, A. Draveny, V. Naletov, L. Vila, J. Attané, C. Beigné, G. de Loubens, M. Viret, N. Beaulieu, J. B. Youssef, *et al.*, Nonlinear spin conductance of yttrium iron garnet thin films driven by large spin-orbit torque, *Phys. Rev. B* **97**, 060409 (2018).
- [9] M. Schneider, T. Brächer, D. Breitbach, V. Lauer, P. Pirro, D. A. Bozhko, H. Y. Musiienko-Shmarova, B. Heinz, Q. Wang, T. Meyer, *et al.*, Bose-einstein condensation of quasiparticles by rapid cooling, *Nat. Nanotechnol.* **15**, 457 (2020).
- [10] M. Weiler, M. Althammer, F. D. Czeschka, H. Huebl, M. S. Wagner, M. Opel, I.-M. Imort, G. Reiss, A. Thomas, R. Gross, *et al.*, Local charge and spin currents in magnetothermal landscapes, *Phys. Rev. Lett.* **108**, 106602 (2012).
- [11] J. S. Jamison, Z. Yang, B. L. Giles, J. T. Brangham, G. Wu, P. C. Hammel, F. Yang, and R. C. Myers, Long lifetime of thermally excited magnons in bulk yttrium iron garnet, *Phys. Rev. B* **100**, 134402 (2019).
- [12] K. S. Olsson, K. An, G. A. Fiete, J. Zhou, L. Shi, and X. Li, Pure spin current and magnon chemical potential in a nonequilibrium magnetic insulator, *Phys. Rev. X* **10**, 021029 (2020).
- [13] L. Cornelissen, J. Liu, R. Duine, J. B. Youssef, and B. Van Wees, Long-distance transport of magnon spin information in a magnetic insulator at room temperature, *Nat. Phys.* **11**, 1022 (2015).
- [14] B. L. Giles, Z. Yang, J. S. Jamison, and R. C. Myers, Long-range pure magnon spin diffusion observed in a nonlocal spin-seebeck geometry, *Phys. Rev. B* **92**, 224415 (2015).
- [15] S. R. Boona and J. P. Heremans, Magnon thermal mean free path in yttrium iron garnet, *Phys. Rev. B* **90**, 064421 (2014).

- [16] F. J. Dyson, General theory of spin-wave interactions, *Phys. Rev.* **102**, 1217 (1956).
- [17] B. Flebus, S. Bender, Y. Tserkovnyak, and R. Duine, Two-fluid theory for spin superfluidity in magnetic insulators, *Phys. Rev. Lett.* **116**, 117201 (2016).
- [18] Our vocabulary distinguishes between thermal magnons, whose energy is $k_B T$, and thermally generated magnons, whose energy covers the spectrum $\lesssim k_B T$.
- [19] $\alpha \sim 10^{-4}$ is a lower bound for the Gilbert damping in YIG thin films with thickness $< 100\text{nm}$.
- [20] V. Cherepanov, I. Kolokolov, and V. L'vov, The saga of yig: spectra, thermodynamics, interaction and relaxation of magnons in a complex magnet, *Phys. Rep.* **229**, 81 (1993).
- [21] J. Plant, Spinwave dispersion curves for yttrium iron garnet, *J. Phys. C: Solid State Phys.* **10**, 4805 (1977).
- [22] J. Barker and G. E. Bauer, Thermal spin dynamics of yttrium iron garnet, *Phys. Rev. Lett.* **117**, 217201 (2016).
- [23] A. Kehlberger, U. Ritzmann, D. Hinzke, E.-J. Guo, J. Cramer, G. Jakob, M. C. Onbasli, D. H. Kim, C. A. Ross, M. B. Jungfleisch, *et al.*, Length scale of the spin seebeck effect, *Phys. Rev. Lett.* **115**, 096602 (2015).
- [24] A. Prakash, B. Flebus, J. Brangham, F. Yang, Y. Tserkovnyak, and J. P. Heremans, Evidence for the role of the magnon energy relaxation length in the spin seebeck effect, *Phys. Rev. B* **97**, 020408 (2018).
- [25] M. Agrawal, V. Vasyuchka, A. Serga, A. Kirihara, P. Pirro, T. Langner, M. Jungfleisch, A. Chumak, E. T. Papaioannou, and B. Hillebrands, Role of bulk-magnon transport in the temporal evolution of the longitudinal spin-seebeck effect, *Phys. Rev. B* **89**, 224414 (2014).
- [26] J. Shan, L. J. Cornelissen, N. Vlietstra, J. B. Youssef, T. Kuschel, R. A. Duine, and B. J. Van Wees, Influence of yttrium iron garnet thickness and heater opacity on the nonlocal transport of electrically and thermally excited magnons, *Phys. Rev. B* **94**, 174437 (2016).
- [27] H. Adachi, K.-i. Uchida, E. Saitoh, and S. Maekawa, Theory of the spin seebeck effect, *Rep. Prog. Phys.* **76**, 036501 (2013).
- [28] L. J. Cornelissen, K. J. Peters, G. E. Bauer, R. Duine, and B. J. van Wees, Magnon spin transport driven by the magnon chemical potential in a magnetic insulator, *Phys. Rev. B* **94**, 014412 (2016).
- [29] N. Beaulieu, N. Kervarec, N. Thiery, O. Klein, V. Naletov, H. Hurdequint, G. de Loubens, J. B. Youssef, and N. Vukadinovic, Temperature dependence of magnetic properties of a ultrathin yttrium-iron garnet film grown by liquid phase epitaxy: Effect of a pt overlayer, *IEEE Magn. Lett.* **9**, 1 (2018).
- [30] R. Kohno, N. Thiery, K. An, P. Noël, L. Vila, V. V. Naletov, N. Beaulieu, J. B. Youssef, G. de Loubens, and O. Klein, Enhancement of yig—pt spin conductance by local joule annealing, *Appl. Phys. Lett.* **118**, 032404 (2021).
- [31] N. Thiery, V. Naletov, L. Vila, A. Marty, A. Brenac, J.-F. Jacquot, G. de Loubens, M. Viret, A. Anane, V. Cros, *et al.*, Electrical properties of epitaxial yttrium iron garnet ultrathin films at high temperatures, *Phys. Rev. B* **97**, 064422 (2018).
- [32] The symmetry argument that is used to distinguish the SSE from SOT is valid i) when the current density is below the non-linear threshold or ii) when spin transport by thermal magnons dominates as in the short range regime, where spin diode effects are negligible.
- [33] Y.-T. Chen, S. Takahashi, H. Nakayama, M. Althammer, S. T. Goennenwein, E. Saitoh, and G. E. Bauer, Theory of spin hall magnetoresistance, *Phys. Rev. B* **87**, 144411 (2013).
- [34] H. Nakayama, M. Althammer, Y.-T. Chen, K. Uchida, Y. Kajiwara, D. Kikuchi, T. Ohtani, S. Geprägs, M. Opel, S. Takahashi, *et al.*, Spin hall magnetoresistance induced by a nonequilibrium proximity effect, *Phys. Rev. Lett.* **110**, 206601 (2013).
- [35] C. Hahn, G. De Loubens, O. Klein, M. Viret, V. V. Naletov, and J. B. Youssef, Comparative measurements of inverse spin hall effects and magnetoresistance in yig/pt and yig/ta, *Phys. Rev. B* **87**, 174417 (2013).
- [36] K. Uchida, S. Takahashi, K. Harii, J. Ieda, W. Koshibae, K. Ando, S. Maekawa, and E. Saitoh, Observation of the spin seebeck effect, *Nature* **455**, 778 (2008).
- [37] M. Gilleo and S. Geller, Magnetic and crystallographic properties of substituted yttrium-iron garnet, $3\text{Y}_2\text{O}_3 \cdot x\text{M}_2\text{O}_3 \cdot (5-x)\text{Fe}_2\text{O}_3$, *Phys. Rev.* **110**, 73 (1958).
- [38] E.-J. Guo, J. Cramer, A. Kehlberger, C. A. Ferguson, D. A. MacLaren, G. Jakob, and M. Kläui, Influence of thickness and interface on the low-temperature enhancement of the spin seebeck effect in yig films, *Phys. Rev. X* **6**, 031012 (2016).
- [39] K. Ganzhorn, T. Wimmer, J. Cramer, R. Schlitz, S. Geprägs, G. Jakob, R. Gross, H. Huebl, M. Kläui, and S. T. Goennenwein, Temperature dependence of the non-local spin seebeck effect in yig/pt nanostructures, *AIP Adv.* **7**, 085102 (2017).
- [40] X. Zhou, G. Shi, J. Han, Q. Yang, Y. Rao, H. Zhang, L. Lang, S. Zhou, F. Pan, and C. Song, Lateral transport properties of thermally excited magnons in yttrium iron garnet films, *Appl. Phys. Lett.* **110**, 062407 (2017).
- [41] V. Castel, N. Vlietstra, J. Ben Youssef, and B. J. van Wees, Platinum thickness dependence of the inverse spin-hall voltage from spin pumping in a hybrid yttrium iron garnet/platinum system, *Appl. Phys. Lett.* **101**, 132414 (2012).
- [42] J. Xiao, G. E. Bauer, K.-c. Uchida, E. Saitoh, S. Maekawa, *et al.*, Theory of magnon-driven spin seebeck effect, *Phys. Rev. B* **81**, 214418 (2010).
- [43] S. A. Bender and Y. Tserkovnyak, Interfacial spin and heat transfer between metals and magnetic insulators, *Phys. Rev. B* **91**, 140402 (2015).
- [44] J. Shan, L. Cornelissen, J. Liu, J. B. Youssef, L. Liang, and B. Van Wees, Criteria for accurate determination of the magnon relaxation length from the nonlocal spin seebeck effect, *Phys. Rev. B* **96**, 184427 (2017).
- [45] Our pulse method, which allows the injection of large current densities in the Pt, does not have the dynamical range to follow the SSE signal at distances above $10\ \mu\text{m}$, where the signal is diminished by three orders of magnitude. This prevents us from studying if there is another tail at this exponential decay with a characteristic length scale of about tens of micron as reported in other studies.
- [46] V. Basso, E. Ferraro, A. Magni, A. Sola, M. Kuepferling, and M. Pasquale, Nonequilibrium thermodynamics of the spin seebeck and spin peltier effects, *Phys. Rev. B* **93**, 184421 (2016).
- [47] S. Hoffman, K. Sato, and Y. Tserkovnyak, Landau-lifshitz theory of the longitudinal spin seebeck effect, *Phys. Rev. B* **88**, 064408 (2013).
- [48] G. A. Slack and D. Oliver, Thermal conductivity of garnets and phonon scattering by rare-earth ions, *Phys. Rev.*

- B **4**, 592 (1971).
- [49] X. Zhang, H. Xie, M. Fujii, H. Ago, K. Takahashi, T. Ikuta, H. Abe, and T. Shimizu, Thermal and electrical conductivity of a suspended platinum nanofilm, *Appl. Phys. Lett.* **86**, 171912 (2005).
- [50] Y. A. Volkov, L. Palatnik, and A. Pugachev, Investigation of the thermal properties of thin aluminum films, *Zh. Eksp. Teor. Fiz* **70**, 2244 (1976).
- [51] S.-M. Lee and D. G. Cahill, Heat transport in thin dielectric films, *J. Appl. Phys.* **81**, 2590 (1997).
- [52] K.-i. Uchida, T. Kikkawa, A. Miura, J. Shiomi, and E. Saitoh, Quantitative temperature dependence of longitudinal spin seebeck effect at high temperatures, *Phys. Rev. X* **4**, 041023 (2014).
- [53] D. G. Cahill, W. K. Ford, K. E. Goodson, G. D. Mahan, A. Majumdar, H. J. Maris, R. Merlin, and S. R. Phillpot, Nanoscale thermal transport, *J. Appl. Phys.* **93**, 793 (2003).